Multipass/Multiview Interferometric SAR

Gianfranco Fornaro
National Research Council (CNR)
Institute for Electromagnetic Sensing of the Environment (IREA)
Via Diocleziano, 328
I-80124 Napoli
ITALY

fornaro.g@irea.cnr.it

ABSTRACT

Synthetic Aperture Radar (SAR) Interferometry is the technique that has significantly pushed the application of SAR remote sensing to many areas of risk monitoring and security. This paper aims to provide an overview of the technique by explaining the basics of SAR interferometry and the recent advances carried out by using multiple pass, through repeated orbits, of SAR sensors to monitor subtle ground deformation. Examples of application of the techniques on real multipass/multiview data are provided to familiarize with the different options provided by SAR Interferometry.

1.0 INTRODUCTION

The principle of synthesis of a large aperture [1] by exploiting the movement of a small real antenna by Carl Wiley in 1951 provided the fundamental basis for the development of microwave high resolution imaging from the space with spatial resolutions comparable with those achieved by optical systems. This element has been the first step in the development and application of Synthetic Aperture Radar (SAR) systems, leading to the recent exponential growth of the launch of satellites carrying on board SAR sensors by the major international Space Agencies.

SAR systems use an own transmitter thus providing day/night operating capabilities; by operating in the microwave spectrum region they allow as well as all-weather imaging capability. SAR sensors transmit a coherent signal, i.e. a signal controlled at the level of a single oscillation. The access to the knowledge of the *phase* provided by the regular oscillation enables the accurate measurement of variations of range to the order of fractions of centimetre by comparing SAR image pairs. The implementation of SAR Interferometry (InSAR) with spatially displaced (across the track) antennas provides angular-view imaging diversity, which allows the SAR system the capability of measuring the "range parallax". Similarly to stereo optical imaging, this solution makes it possible to estimate the target elevation and hence to reconstruct the scene Digital Elevation Model (DEM). The technique, known as across-track SAR Interferometry [2]-[4], is cost effective in terms of accuracy and coverage and has been exploited in 2000 by the Space Shuttle for the generation of the most accurate global DEM known as Shuttle Radar Topography Mission (SRTM) and freely available on the web. The same principle has been exploited by the TerraSAR-X/Tandem-X mission, currently orbiting around the Earth, to provide a global DEM with accuracies significantly better than those of the SRTM mission.

An interesting extension of across track InSAR is the Differential SAR Interferometry (DInSAR) technique. It is based on the acquisition of images relative to the same scene at different times by repeated passes [5]: by exploiting the phase difference of the image pair DInSAR allows measuring surface displacements occurring between the two acquisition dates with an accuracy of the order of fractions of the wavelength (a few centimetres for C-band and X-band sensors). DInSAR has dramatically increased the application of SAR imaging to many areas of natural and human induced risk monitoring and security. Since its first demonstration with data from the European Remote Sensing Satellite (ERS) in for ice-stream velocity measures in Antarctica [6] and in [7] for the co-seismic deformation field generated by the Landers

earthquake many other applications to the study of earthquakes, volcanoes, landslides, etc. have been carried out in the past years. The intense application of DInSAR has increased the interests of the major international space Agencies in the development and launch of spaceborne SAR sensors satellites. Following the twin satellites ERS-1 and ERS-2 of the European Space Agency (ESA), operative (at C-band) in total from 1992 to September 2011, many other missions have been successfully developed. This is the case of the C-band SAR sensors on board ENVISAT (2002-2012), RADARSAT-1 (2001-2013) and RADARSAT-2 (in orbit from 2007) sensors by the Canadian Space Agency and L-band SAR sensor ALOS-PALSAR (2006-2011) by the Japanese Space Agency. Above all, SAR sensors have provided long-term archives of regularly acquired data, with highest temporal sampling rate of typically one image every 20-30 days, which have been used for the experimental implementation and development of classical DInSAR techniques. Advanced DinSAR (A-DInSAR) algorithms are able to achieve very accurate monitoring of ground deformations by jointly and coherently processing stacks of SAR data. Data by the past generation satellites have been integrated by the new high and very high resolution SAR sensor able to reach meter and sub-meter resolution to provide information about deformation of single ground structure. The Italian COSMO-SkyMed (CSK) constellation and German TerraSAR-X [TSX] missions, recently launched in 2007, have dramatically improved the quality of the available SAR data with resolutions reaching the order of 1m. The CSK mission provides, worldwide, a unique constellation of SAR sensors composed of four medium-size satellites, each one equipped with an X-band high-resolution SAR system, allowing acquiring images on the same area by repeating orbits up to one image every 4 days (on average).

This paper aims to provide a discussion about the principles of SAR interferometry and of advanced multipass/multiview interferometric SAR processing.

2.0 BASICS OF SAR INTERFEROMETRY

2.1 Interferometric for Height Retrieval

SAR imaging allows discrimination of targets along the azimuth and range directions. Assuming SAR sensors to fly locally rectilinear trajectories (airborne) or orbits (space borne), two coordinates are identified: the azimuth directed along the sensor velocity vector and the range, i.e. the distance from the flight track. Azimuth and range represent the two coordinates of a cylindrical reference system with the axis coincident with the flight track, which is the natural radar reference system. A single SAR image, for instance acquired by sensor S_1 in Figure 1, is insufficient to provide the knowledge about the angle ϑ, usually referred to as look angle, under which a target at range r is imaged. The target could be in principle one of the points located on the equi-range curve (red curve in Figure 1) at range r.

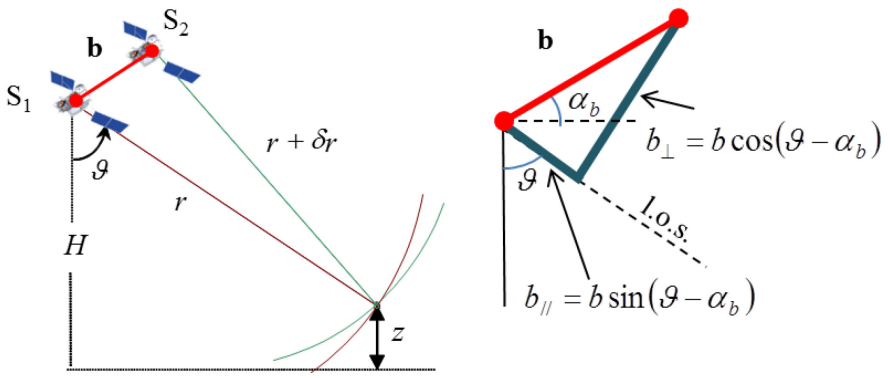

Figure 1: Reference Geometry for SAR Interferometry. Left image: Geometry of the interferometric SAR acquisition in the plane orthogonal to the flight direction. Right image: Relevant to the decomposition of the baseline parallel and perpendicular to the target line of sight (l.o.s.).

The information about the look angle can be extracted by exploiting at least two SAR images acquired under angular imaging diversity along the vertical direction, see Figure 1. The concept is very similar to the principle of the human eyes: the provision of images acquired under angular diversity at the two eyes allows sensing the depth of the scene. In SAR interferometry, the use of at least two images acquired from slightly different observation positions allows measuring the two range of the target at the first and second antenna: the target is therefore located at the intersection of the two equi-range (red and green curve).

Similarly to human eyes which determines the variation (parallax) of the projection of the object at the two eyes to measure the depth, the key quantity that allows radars achieving the sensitivity to the target height (z) is δr, i.e. the range (travelled path) variation from one image to the other [5]:

$$\begin{cases} \delta r \cong -b\sin\left(\vartheta - \alpha_b\right) = -b_{//} \\ z = H - r\cos\vartheta \end{cases} \tag{1}$$

where α_b is referred to as tilt angle and H is the satellite height.

The sensitivity of the system to height variations is:

$$\frac{\partial \delta r}{\partial z} = \frac{\partial \delta r}{\partial \vartheta}\frac{\partial \vartheta}{\partial z} = -\frac{b\cos\left(\vartheta - \alpha_b\right)}{r\sin\vartheta} = -\frac{b_{\perp}}{r\sin\vartheta} \tag{2}$$

Equation (2) provides the indication that what really matters for the systems sensitivity to the height is the component of the baseline orthogonal to the target line of sight (l.o.s.). The sensitivity increases with $b_{\perp}$ and decreases with the range distance (r). Being typically r large, especially for satellite systems, a high accuracy on the determination of δr is needed for limiting errors on the determination of z.

Determination of δr with accuracies of some (few) fractions of the resolution cell, such as those achieved via techniques that carries out image cross-correlation between the master (S_1) and slave (S_2) images (referred to as stereometric techniques and widely used in optical topography reconstruction), would lead, especially for systems with medium range resolution, to an insufficient height accuracy. Propagation of electromagnetic waves is known to introduce phase variation proportional to the travelled path. Accordingly, to tackle the above problem, SAR interferometry exploits the phase difference extracted from the interference of the two images after proper alignment (registration) aimed at allowing the correct (geometrical) overlap of the slave image onto the master image. Being phase variations occurring on the scale of the wavelength (λ), such technique makes it possible to measure δr with accuracies that are fractions of the wavelength.

In fact, letting:

$$\hat{\gamma}_1 = \gamma_1 e^{-j\frac{4\pi}{\lambda}r} \quad \hat{\gamma}_2 = \gamma_2 e^{-j\frac{4\pi}{\lambda}(r+\delta r)} \tag{3}$$

to be the two (complex) images at the first and second antenna of the same target, under the assumption that:

$$\gamma_1 = \gamma_2 \tag{4}$$

i.e. that the target reflectivity γ seen at the first (γ_1) and second antenna (γ_2) are equal, it results that:

$$\delta r = \frac{\lambda}{4\pi}\varphi \tag{5}$$

where the interferometric phase φ is:

$$\varphi = \mathrm{Arg}\left[\hat{\gamma}_1 \hat{\gamma}_2^*\right] \tag{6}$$

$\mathrm{Arg}[\cdot]$ being the function that extracts the (unrestricted) argument of a complex number. What is however really measured is the restricted argument of φ, i.e., $\phi = \arg\left[\hat{\gamma}_1 \hat{\gamma}_2^*\right]$ which belongs to the $(-\pi, \pi)$ interval and an operation, referred to as phase unwrapping is necessary to retrieve the absolute phase φ [8]-[10].

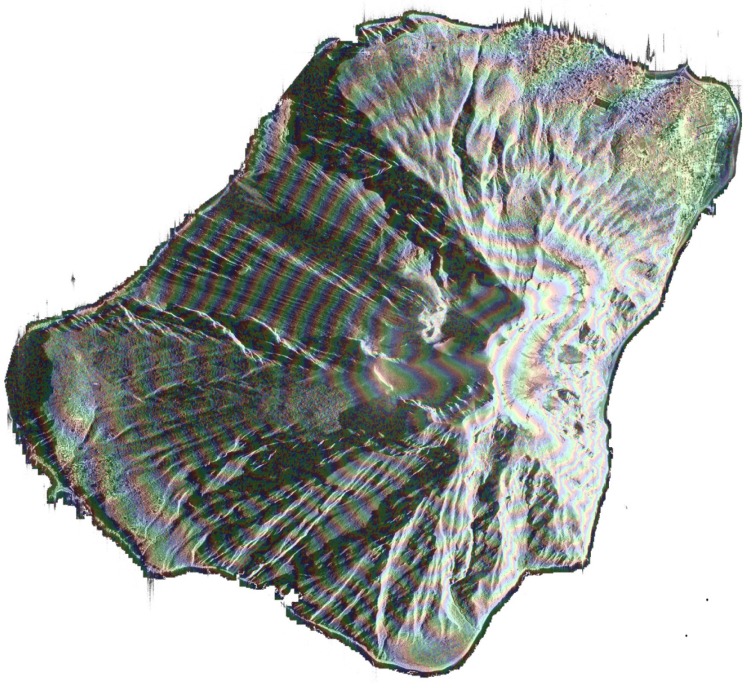

Figure 2: Overlay of the Wrapped Phase and Amplitude SAR Images Over the Stromboli Island Showing How the Phase Itself Provides Indication of the Topography of the Scene. The data have been acquired by the COSMO/SKYMED system.

The height variation that generates a phase change of 2π is called ambiguity height ($z_{2\pi}$). From (2) and (5) it follows that:

$$z_{2\pi} = \frac{\lambda r \sin \vartheta}{2 b_\perp} \tag{7}$$

Accordingly, larger baselines correspond to lower ambiguities height and therefore to a densification of the fringes that allows achieving higher accuracy in the DEM reconstruction, see (2) and (7). Nevertheless, besides making phase unwrapping more challenging a baseline increase also leads to an increase of the noise, as described in the next section.

2.2 Decorrelation in SAR Interferometry

The assumption in equation (4) is fundamental for the cancellation of the phase of scene backscattering in the hermitian product in (6). Changes in the relative phase of γ_1 and γ_2 leads to the presence of noise contribution in the interferometric phase φ which is referred to as decorrelation. To measure the degree of

decorrelation, it is introduced the cross-correlation index χ, which is a measure of the linear predictability of one random variables with respect to the other:

$$\chi = \frac{\mathrm{E}\left[\hat{\gamma}_1 \hat{\gamma}_2^*\right]}{\sqrt{\mathrm{E}\left[\left|\hat{\gamma}_1\right|^2\right]\mathrm{E}\left[\left|\hat{\gamma}_2\right|^2\right]}} = \rho \exp\left(j\frac{4\pi}{\lambda}\delta r\right) \tag{8}$$

The modulus of χ, ρ belongs to the interval $[0,1]$ and is referred to as coherence. The closer the coherence to 1, the higher the correlation degree and therefore the lower the noise contribution [11]. Accordingly, $1-\rho$ is the decorrelation degree between the two acquisitions. The cases $\rho = 0$ and $\rho = 1$ leads to a probability density function of the measured phase which is uniformly distributed in $(-\pi, \pi)$ and Dirac impulsive, respectively. Further details on the statistical distribution of the phase can be found in [3], [5] and [12].

The coherence is a product of several decorrelation factors [11], one of the most important being associated with the change of the imaging geometry ($\rho_{spatial}$) due to the spatial orbit offset (spatial baseline or simply baseline), the (possible) temporal separation between the acquisitions ($\rho_{temporal}$) and the thermal noise.

$$\rho = \rho_{spatial}\rho_{temporal}\rho_{thermal} \tag{9}$$

Spatial decorrelation is due to the fact the scattering from a resolution cell typically involves the integration of a large number of scattering centres: the change of the imaging angle determines a change (also in phase) of the backscattering coefficient (speckle decorrelation).

For a white scene, i.e. when the process γ describing the scene backscattering is characterized by an impulsive autocorrelation (absence of correlation between different scatterers), it can be shown that the decorrelation is due (on flat terrain) to a spectral shift of reflectivity spectrum [13]. In this case, letting B_r be the spatial range bandwidth [m^{-1}] it result that:

$$\rho_{spatial} = \left(1 - \frac{|\xi_0|}{B_r}\right) \quad \text{for } |\xi_0| \le B_r \text{ and 0 elsewhere} \tag{10}$$

$$\xi_0 = \frac{2b_\perp}{\lambda r_0}\cot(\vartheta - \beta) \tag{11}$$

where r_0 is the scene range and β is the terrain slope. It is evident that, the larger the baseline the lower the spatial coherence; moreover, the closer β is to ϑ ($\beta = \vartheta$ is the layover limit) the lower is the spatial coherence. The value of $b_\perp$ that leads to $\xi_0 = B_r$ is called critical baseline ($b_{\perp c}$); it turns out that

$$b_{cr} = \frac{\lambda r_0 B_r}{2\cot(\alpha - \beta)} = \frac{\lambda r_0}{2\Delta r \cot(\alpha - \beta)} \tag{12}$$

where $\Delta r = 1/B_r$ is the range resolution. For the ERS and ENVISAT (C-Band) systems the critical baseline is slightly above 1Km, for CSK (X-Band) the critical baseline is above 4Km.

The spatial decorrelation can be contrasted by implementing a proper filtering, which is stationary for a planar terrain [13] and non-stationary for a rolling topography [14]. This filtering is effective on distributed

scattering, such as that associated with rural area; it is, however, not recommended in urban areas where the presence of dominant scatterers centres leads to the presence of a degree of correlation in the backscattering harmonics [14].

The temporal decorrelation is due to the change of the scene backscattering properties over the time. This decorrelation source is of main importance in repeat pass interferometry, especially with systems operating at higher frequencies (f.i. X-band). It is critical over the sea and in vegetated area where the growth and in general the change of vegetation leads to strong variation of the backscattering coefficient. Temporal decorrelation is, generally, modelled with an exponential decay time law [11], where the decay constant depends mainly on the scene and the land coverage.

The last term, thermal decorrelation, is due to the presence of thermal noise in the receiving apparatus. It is particularly evident in areas characterized by very low scene backscattering [3]. Other decorrelation sources are associated with variations of the imaging aspect angle (Doppler Centroid decorrelation) and to processing artefacts [3], [11].

The correlation index and hence the coherence can be estimated on real data by substituting the statistical averaging with a spatial multilooking: modern algorithms use advanced (adaptive) spatial multilooking to account for non-stationary (inhomogeneous) backscattering. After multilooking the phase of the correlation index is assumed as multilook phase in which the noise content is reduced.

2.3 Differential SAR Interferometry

Differential Interferometry (DInSAR) is a particular configuration of SAR interferometry where the interferometric acquisitions are obtained by two repeated passes over the same orbit [16]. The reference geometry is the same of the classical InSAR case in Figure 1 with the difference that the target on the ground is allowed to move between the acquisition epochs.

With reference to Figure 3 let us indicate with **d** the displacement vector between the two passes; the interferometric phase can be assumed composed of three main factors:

$$\varphi = \frac{4\pi}{\lambda}\delta r = \frac{4\pi}{\lambda}\delta r_d + \frac{4\pi}{\lambda}\delta r_z + \varphi_a + \varphi_n, \tag{13}$$

where δr_z is the contribution associated with the topography described in Sect. 2.1 (i.e. due to the difference between the green and red range lines in Figure 3) vanishing for $\mathbf{b} = 0$; φ_n is a stochastic term associated with the phase noise including thermal, spatial and temporal decorrelation (see Sect. 2.2). It is worth noting that, being differential acquisitions often acquired also with large temporal separations, the effect of temporal decorrelation is typically the main source of noise.

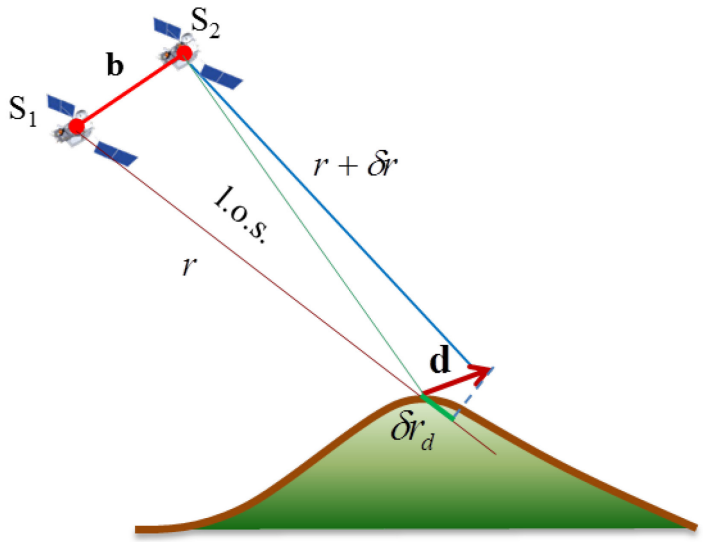

Figure 3: Reference Geometry for Differential SAR Interferometry. The target is moving between the times corresponding to the two acquisitions carried out at different times.

Equation (13) includes two additional terms with respect to the components previously analysed in Sect. 2.1: both terms are associated with the fact that acquisitions are carried out at different times (epochs). First of all, when wave propagate through the atmosphere they are delayed according to the refraction index [17]: the delay is interpreted as an increase of the range, which in turn produces a variation of the phase. Such a phase affects in the same way the two images in simultaneous acquisitions: it, thus, cancels at the signal beating stage for the extraction of the interferograms. In repeat pass acquisitions with temporal difference typically larger from days to years, the refraction index shows significant variations: φ_a is therefore the phase associated with variation of the atmosphere between the two acquisitions. Such term can be stochastically characterized [17] and typically shows (at C-Band) spatial variations within the scale of a few hundreds of meters and magnitudes of the order of a few (typically <3,4) multiples of 2π. Secondly, there is the presence of the range variation associated to a displacement on the ground δr_d: it is noted that, at large range, δr_d (the variation associated with the green and blue lines in Figure 3) is approximately equal to the component of the displacement vector **d** along the radar l.o.s.

In order to estimate δr_d, in differential interferometry, the original interferogram is processed to subtract the component associated with the topography evaluated from an external DEM (typically the SRTM DEM): such operation, referred (together with the registration) to as zero baseline steering, aims at eliminating the fringes corresponding to the topography contribution usually referred to as "synthetic fringes":

$$\varphi_d = \varphi - \frac{4\pi}{\lambda}\hat{\delta r}_z = \frac{4\pi}{\lambda}\delta r_d + \varphi_a + \varphi_n, \tag{14}$$

where $\hat{\delta r}_z$ is the range variation associated with the scene topography estimated from the available DEM.

For a successful removal of such a contribution, the DEM must be sufficiently accurate. It is however to be noted that the accuracy depends in any case on **b**, indeed on $b_\perp$: the smaller $b_\perp$ the less is the influence of the topography and therefore the less stringent is the accuracy of the DEM. For such a reason acquisitions with small orbital separation are preferred in DInSAR analysis: this solution leads as well as to a benefit also in terms of phase noise induced by the spatial decorrelation.

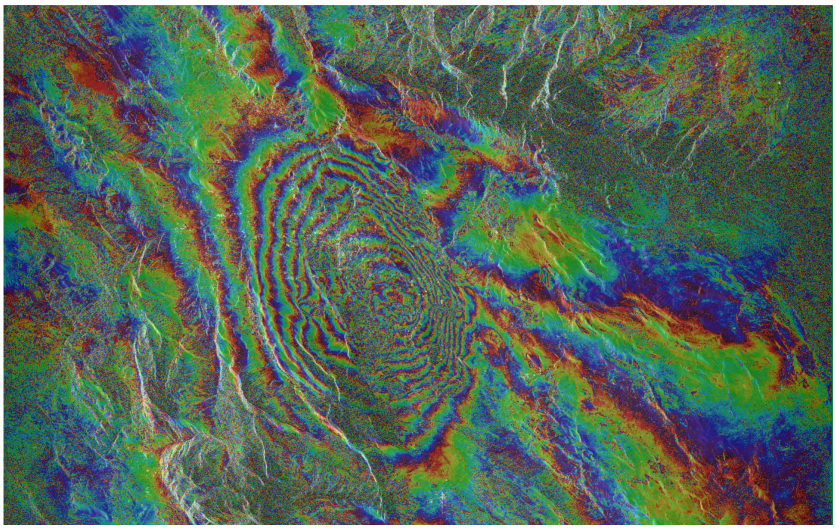

Figure 4: Differential Interferogram Associated with the Main Shock of April 6th 2009 in the l'Aquila Earthquake Sequence: each fringe (change of colour from blue to red) corresponds to a lowering of the surface area of about 2cm: the total subsidence is more than 20cm. Images were acquired by the COSMO/SKYMED constellation on 4th and 12th of April 2009.

In the case of a predominance of the deformation component and/or limited effects of atmospheric variation, the displacements δr_d can be measured to an accuracy level of the order of the wavelength. By using this classical two passes DInSAR configuration geophysicists have been able in many case to capture surface deformation field generated by major earthquakes or to highlight deformation associated with volcanic activities. DInSAR deformation patterns have been used in conjunction with available geophysical models to inferring the rupture pattern (dip) on the fault plane or estimate the magma source shape and its movements, respectively.

3.0 MULTIPASS/MULTIVIEW SAR INTERFEROMETRY

Satellites are able to repeat orbits regularly over the time. Consequently, stacks of multipass acquisitions, characterized by angular and temporal diversity, are available in remote sensing archives for many areas of the Earth surface. In order to achieve a higher accuracy in the estimation of the deformation modern A-DInSAR processing algorithm jointly processes all the images in stacks of multitemporal acquisitions: this processing allows in fact discriminating between the atmospheric and deformation phase components as well as the topography contribution.

In the literature two different classes of A-DinSAR algorithms are typically used: Coherence Stacking Interferometry (CSI) [18]-[20] and Persistent Scatterers Interferometry (PSI) [21], [22]. The first class of algorithms make use of spatial multilooking to estimate the coherence and to reduce the phase noise in interferograms via averaging: spatial multilooking allows also to down sample the data in azimuth and range and therefore this class of algorithms is particularly suitable for the analysis of wide areas at lower resolution (small scale). To this class of algorithms belongs the well-known Small Baseline Subset (SBAS) approach in [18] for which the interferograms are generated by bounding the spatial and temporal separation (baseline) between the acquisition pairs to limit the spatial decorrelation associated with distributed scattering. The second class of algorithms on the contrary analyses interferograms at the highest spatial resolution to determine the deformation of single dominant scatterers, typically associated to man-made structures (dihedral and trihedral of walls edges, masts, gratings, etc.). In this case, to achieve also high accuracy in the estimation of the localization of scatterers, no limitations on the spatial baseline are introduced. To this class of algorithms belong the Persistent Scatterers (PS) techniques [21], [22].

3.1 Coherence Stacking Interferometry

Let us refer to Figure 5 where it is assumed that the satellite is collecting the N images at ordered time instants (epochs), collected in the vector $\mathbf{t}=[t_1...t_N]^{\mathrm{T}}$ (T is the transpose operator) also referred to as temporal baselines, and (spatial) baselines, collected in the vector $\mathbf{b}_{\perp}=[b_{\perp 1}...b_{\perp N}]^{\mathrm{T}}$: spatial and temporal baselines are referred to a reference (master) image (for example the first image). Following the step that register all images with respect to the master image [23], a set of say M interferograms, spatially multilooked, is generated from the acquisitions. In the following the symbol "Δ" is introduced to identify quantities that refer to interferometric pairs. For each azimuth and range pixel, we can therefore define the M-dimensional vector $\Delta\boldsymbol{\varphi}$ collecting all interferometric (unwrapped) measurements:

$$\Delta\boldsymbol{\varphi}=\frac{4\pi}{\lambda}\frac{\Delta\mathbf{b}_{\perp}}{r}e_s+\frac{4\pi}{\lambda}\Delta\mathbf{d}_{los}+\Delta\boldsymbol{\varphi}_{atm}+\Delta\mathbf{n} \tag{15}$$

where $\Delta\mathbf{b}_{\perp}/r$ is a M-dimensional vector of parameters that collect the angular variations corresponding to the spatial baselines of the interferograms (collected in $\Delta\mathbf{b}_{\perp}$), $e_s=e_z/\sin\vartheta$ with e_z being the error in the external DEM, $\Delta\mathbf{d}_{los}$ is the vector collecting the variations of the displacement on the acquisition pairs; $\Delta\boldsymbol{\varphi}_{atm}$ collects the phase due the variation of the APD on the interferometric pairs.

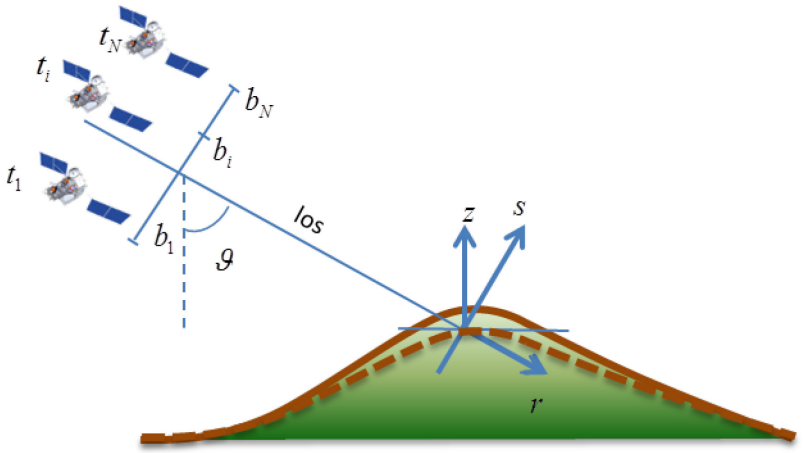

Figure 5: Reference Geometry for Multipass Differential SAR Interferometry. Continuous and dashed terrain profiles correspond to the true and available (inaccurate) Digital Elevation Model (DEM).

A key feature of the Advanced DInSAR techniques based on the processing of stack of multitemporal data is associated with the possibility to separate the different components in (15), e_s, $\Delta\mathbf{d}_{los}$ and $\Delta\boldsymbol{\varphi}_{atm}$, by exploiting their deterministic/statistical properties as explained in the following.

The residual topography e_s (a scalar quantity) is estimated by considering that the vector $\Delta\mathbf{b}_{\perp}/r$ is known from the orbital state vectors (satellite positions). The first (vector) component in (15) has a well-known structure (signature) that follows precisely the spatial baseline distribution: it can be therefore estimated by tacking the scalar product between $\Delta\boldsymbol{\varphi}$ and (a properly scaled version) of $\Delta\mathbf{b}_{\perp}/r$. It is worth noting that in CSI approach, due to the limitation on the spatial baselines, this contribution is in general marginal.

After the cancellation of the first contribution, i.e. $\Delta\boldsymbol{\varphi} \leftarrow \Delta\boldsymbol{\varphi} - \frac{4\pi}{\lambda}\frac{\Delta\mathbf{b}_{\perp}}{r}\hat{e}_s$, the interferometric phase values are inverted to reconstruct the N-dimensional phase vector $\boldsymbol{\varphi} = [\varphi_1 .... \varphi_N]^{\mathrm{T}}$ collecting the phase of the N acquisitions ordered accordingly to the time instants $t_1, t_2, \ldots\ldots, t_N$. To this end, it is introduced the following incidence matrix describing the pairing between the acquisitions for the interferogram generation, i.e. the graph in the acquisition domain where the arcs are the interferometric pairs and the end nodes the acquisitions:

$$\mathbf{A} = \begin{bmatrix} 0 & -1 & 0 & +1 & \ldots \\ 0 & 0 & +1 & 0 & \ldots \\ \ldots & \ldots & \ldots & \ldots & \ldots \\ \ldots & \ldots & \ldots & \ldots & \ldots \end{bmatrix} \tag{16}$$

Each row of the MN matrix $\mathbf{A}$ describes one interferogram pair with +1 and -1 located at the position of the second and first acquisition of the interferogram. Concisely, we have:

$$\mathbf{A}\boldsymbol{\varphi} = \Delta\boldsymbol{\varphi} \tag{17}$$

Inversion of (17) can be carried out pixel by pixel by introducing the initial condition $\varphi_1 = 0$ in each pixel (φ_1 being the first element of $\boldsymbol{\varphi}$). As it is generally $M>N$ (redundancy of interferograms), this inversion is generally carried out in the Least Square sense via the use of the pseudo-inverse [24]. In cases in which the acquisition graph is disconnected, the Singular Value Decomposition technique may be used to "pick up" the most suitable solution with the minimum kinetic energy [24], [18].

After the inversion the following vector composition should be considered in place of (15):

$$\boldsymbol{\varphi} = \frac{4\pi}{\lambda}\mathbf{d}_{los} + \boldsymbol{\varphi}_{atm} + \mathbf{n} \tag{18}$$

where $\mathbf{d}_{los}$ and $\boldsymbol{\varphi}_{atm}$ are the displacement (time series) and APD vectors ordered with respect to the acquisition time. The separation between the displacement and APD vectors is carried out by considering their statistical characterization in terms of spatial and temporal variability: $\mathbf{d}_{los}$ shows typically a spatial and temporal correlation whereas $\boldsymbol{\varphi}_{atm}$ is correlated along the space but uncorrelated with respect to the time. Accordingly, a simple spectral filtering implemented in the wavenumber/frequency domain is typically sufficient to achieve the measurement of the time series in each pixel.

It is worth pointing out that the most critical part of the processing procedure is represented by the unwrapping step. A correct unwrapping is fundamental to preserve the spectral characteristics of the signal, which is fundamental for the separation of the different components. The unwrapping is, therefore, carried out on a suitable sparse grid where the phase information is less affected by noise: to this end, the available coherence stack is used to identify reliable and noisy areas. After the unwrapping a further check is carried out by analysing the residual between the starting (wrapped interferograms) and $\mathbf{A}\left(\mathbf{A}^T\mathbf{A}\right)^{-1}\mathbf{A}^T\Delta\boldsymbol{\varphi}$; note that $\mathbf{A}\left(\mathbf{A}^T\mathbf{A}\right)^{-1}\mathbf{A}^T$ is the projector onto $\mathcal{R}(\mathbf{A})$, i.e. the range (space) of the matrix $\mathbf{A}$. Modern phase unwrapping algorithms do not carry out the unwrapping of each interferogram separately but try to solve (compatibly with the computational costs) the joint phase unwrapping of all the interferograms [25].

To show the potentialities of the A-DInSAR processing in Figure 6 results achieved by processing real CSK data are displayed. The results are achieved by processing 33 stripmap acquisitions relative to the beam 09

(Incidence Angle ~ 40.1°) on ascending passes acquired between April 4th and October 13th 2009 [26], [27]. The CSK constellation (at that time with 3 of the 4 satellites now in orbit) intensified the acquisition to its highest possible rate (almost 1 acquisition every 5 days on average). The velocity map (evaluated only the post-seismic dates from April 12th to October 13th) overlaid to a Google in Figure 6 shows an area of subsidence with a rate exceeding the limit of 6cm/yr. In the same image, the plot of the time series of a point in the Paganica area show the jump associated to the main shock (April 6th) and the exponential decay of the subsidence with the aftershocks.

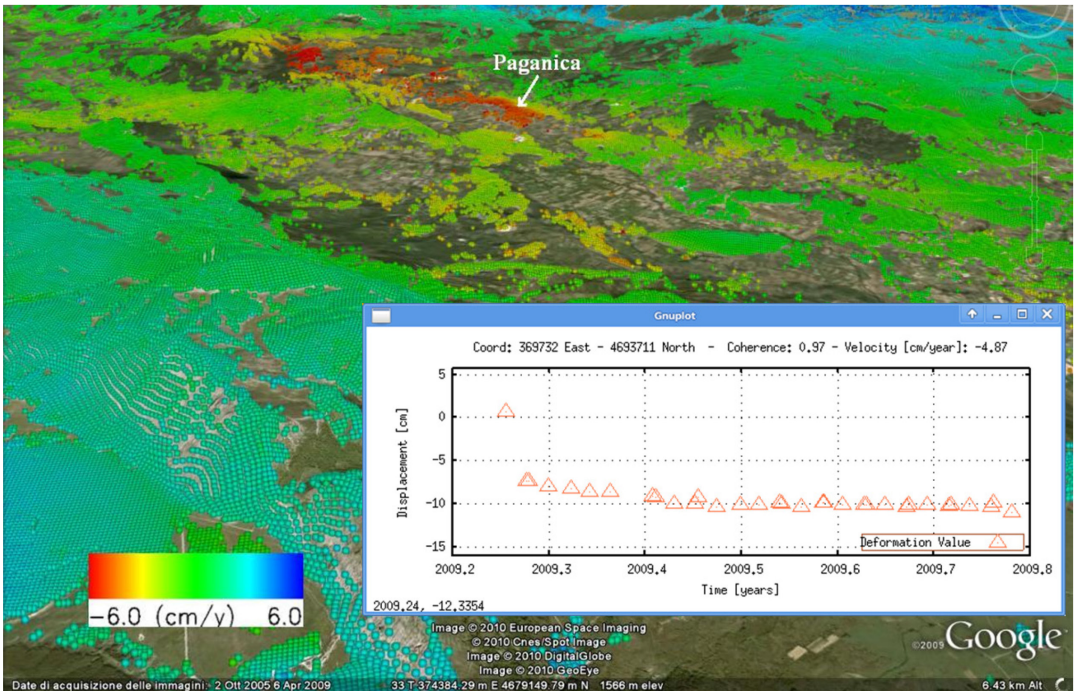

Figure 6: Example of Estimation of the Post-Seismic Velocity Map and of the Co/Post-Seismic Time Series of a Point in the Paganica Area Close to l'Aquila Obtained by Processing a Dataset of 33 COSMO/SKYMED Images Acquired Between April 4th and October 13th 2009.

Advanced techniques that exploit both the amplitude (coherence) and phase (multilook phase) of the correlation index matrix, such as SQUEESAR [28] or CAESAR [29] can be used to significantly improve the results of the processing.

3.2 Persistent Scattering Interferometry

Persistent Scattering Interferometry is tailored to the analysis of man-made structures. It carries out an analysis of data at full resolution (i.e. without any spatial multilooking) and makes use of a model to determine (by exploiting the multiview nature of available stacks) the accurate residual topography necessary to correctly localize the scatterer centre on the investigated target and to monitor its temporal evolution by exploiting the multitemporal characteristic of multipass data. The use of the model however presumes the compensation of phase contributions such as the APD disturbance. Such a compensation can be carried out either by analysing the phase on Persistent Scatterers (PS) candidates, that is strong scatterers where the phase is less affected by noise, or by using the low-resolution product (φ_{atm}) of CSI techniques discussed in the in Sect. 3.1. In the latter case, a good practice is also to subtract the low resolution deformation $\mathbf{d}_{los}$ so to obtain a steering to zero of the phase (spatial and temporal zero baseline steering) in such a way that the high resolution analysis is carried out only the on residual phase signals.

Following this compensation, deformations are divided into the linear (slope of the time series wrt to the epochs) and non-linear addenda; the following model is assumed for be compensated phase at full resolution ($\boldsymbol{\phi}$):

$$\boldsymbol{\phi} = \frac{4\pi}{\lambda} v\mathbf{t} + \frac{4\pi}{\lambda}\frac{\mathbf{b}_{\perp}}{r}s + \mathbf{d}_{nl} + \mathbf{n} \tag{19}$$

where v is the (l.o.s.) average (mean) velocity of the pixel (residual with respect to the low resolution if compensation for $\mathbf{d}_{los}$ at small scales has been carried out) $s = z/\sin\vartheta$ is the residual (wrt the external DEM) elevation of the scatterer and $\mathbf{d}_{nl}$ is the (l.o.s.) non-linear deformation addendum (again residual with respect to the low resolution if compensation for $\mathbf{d}_{los}$ at small scales has been carried out).

It is worth noting that, to achieve high accuracy in the topography estimation and to exploit the angular correlation properties of strong scatterers, the PSI approach does not impose any predefined limit on the spatial baseline.

PSI techniques assumes $|\mathbf{d}_{nl}| << 1$ and estimates, pixel by pixel at full resolution, v and s by analysing the following normalized, in the (0-1) interval, index measuring the un-modelled residues [21], [22]:

$$C(s,v) = \frac{1}{N}\left|\sum_{i=1..N} e^{j\varphi_i - j\frac{4\pi}{\lambda}(\xi_i s + t_i v)}\right| \tag{20}$$

This quantity is a measure of temporal coherence (i.e. persistent) property of the scatterers: s, i.e. the scatterer (residual wrt to the external DEM) elevation, and v (residual wrt to the low-resolution deformation) velocity are determined via the following maximization:

$$(\hat{s},\hat{v}) = \arg\max_{s,v} C(s,v) \tag{21}$$

which is typically solved with and exhaustive search in a predefined interval. Only pixels for which $C(\hat{s},\hat{v})$ is above a fixed threshold are labelled as persistent scatterers and therefore the algorithm provides the temporal series as a product.

Figure 7 shows a deformation mean velocity map at full resolution, obtained by processing with a PSI approach of 43 images acquired by ERS-1 and ERS-2 sensors in the period from 1995 to 2000, overlaid to a Google map. It is to be noted the accurate localization of scatterers on man-made structures (building, railway tracks, etc.) which is the result of a very precise (typically on the order of a few meters) estimation of the elevation (s) at full resolution provided by the exploitation of all available spatial baselines (dataset multiview characteristic).

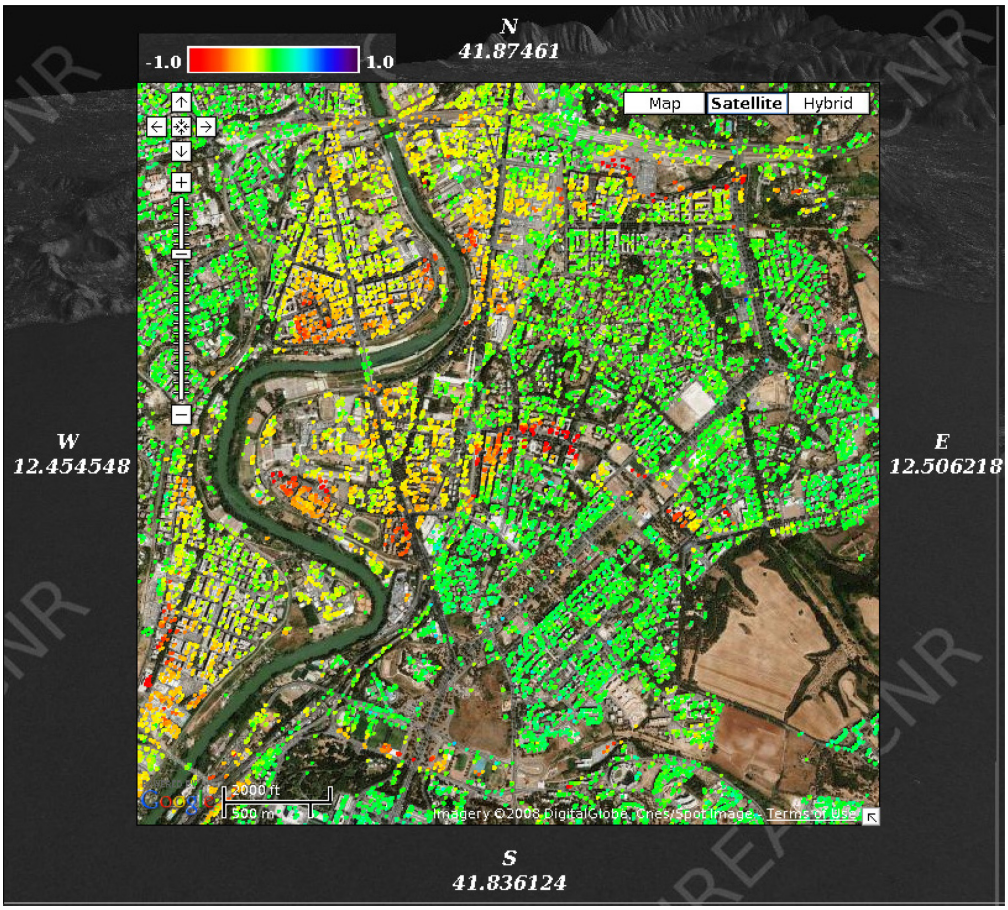

Figure 7: Example of Estimation of the Full Resolution Deformation on Structures in Rome in an Area Close to the Tevere River.

PSI exploits only the phase information to estimate the target parameters, see (20) and (21), moreover PSI assumes the presence of only one (dominant) scatterer in each resolution cell. These limitations lead to a loss of performances in areas where layover is frequent (f.i. urban areas) and can be talked by using SAR Tomography.

4.0 ACKNOWLEDGMENTS

The author wish to thank the European Space Agency (ESA), the Italian Space Agency (ASI) and the Department of Civil Protection within framework of the l'Aquila earthquake emergency for providing access to data used in this paper. Many thanks go also to Diego Reale and Carlo Noviello for the paper proofread.

5.0 REFERENCES

[1] C. A. Wiley, "Synthetic Aperture Radars: A Paradigm for Technology Evolution", IEEE Transactions on Aerospace and Electronic Systems, 21(3), pp. 440-443, 1985.

[2] P. A. Rosen, S. Hensley, I. R. Joughin, F. K. Li, S. N. Madser, E. Rodriguez, R. M. Goldstein, "Synthetic Aperture Radar Interferometry", Proc. of IEEE, 88(3), pp. 333-382, 2000.

[3] R. Bamler, P. Hartl, Synthetic Aperture Radar Interferometry, Inverse Problems, 14, pp. R1-R54, 1998.

[4] G. Fornaro, V. Pascazio, SAR Interferometry and Tomography: Theory and Applications, Academic Press Library in Signal Processing Volume 2, Elsevier Ltd. 2013.

[5] G. Fornaro, G. Franceschetti, "SAR Interferometry", Chapter IV in G. Franceschetti, R. Lanari "Synthetic Aperture Radar Processing", CRC-PRESS, Boca Raton, Marzo 1999.

[6] R.M. Goldstein, H. Engelhardt, B. Kamb, R.M. Froclich, "Satellite RADAR interferometry for monitoring ice-sheet motion—application to an Antarctic ice stream", Science 262 (5139), pp. 1525-1530, 1993.

[7] D. Massonnet, M. Rossi, C. Carmona, F. Adragna, G. Peltzer, K. Feigl, T. Rabaute, "The displacement field of the Landers earthquake mapped by radar interferometry", Nature, 364(6433), pp. 138-142, 1993.

[8] M. Costantini, "A Novel Phase Unwrapping Method Based on Network Programming", IEEE Trans. Geosci. Remote Sens., 36(3), pp. 813-821, 1998.

[9] D. C. Ghiglia, M. D. Pratt, "Two-Dimensional Phase Unwrapping, Theory, Algorithms, and Software", Wiley-Interscience, New York (USA), 1998, ISBN 0-471-24935-1.

[10] C. W. Chen, H. A. Zebker, "Two-dimensional phase unwrapping with use of statistical models for cost functions in nonlinear optimization," Journal of the Optical Society of America A, Vol. 18, pp. 338-351, 2001.

[11] Zebker S. H. A., J. Villasenor , "Decorrelation in Interferometric Radar Echoes", IEEE Trans. Geosci. Remote Sens., 30, 950-959, 1992.

[12] Touzi R., A. Lopes, J. Bruniquel, P. W. Vachon, Coherence Estimation for SAR Imagery, IEEE Trans. Geosci. Remote Sens., 37, pp. 135-149, 1999.

[13] F. Gatelli, F., A. Monti Guarnieri, F. Palizzi, P. Pasquali, C. Prati, F. Rocca, "The wavenumber shift in SAR interferometry", IEEE Trans. Geosci. Remote Sens., 32, pp. 855-865, 1994.

[14] G. Fornaro, A. Monti Guarnieri, "Minimum Mean Square Error Space-Varying Filtering of Interferometric SAR Data", IEEE Trans. Geosci. Remote Sens., 40, pp. 11-21, 2002.

[15] C.A. Deledalle, L. Denis, F. Tupin, "NL-InSAR: Nonlocal Interferogram Estimation", IEEE Trans. Geosci. Remote Sens., 49 (4), pp. 1441-1452, 2011.

[16] A. K. Gabriel, R. M. Goldstein, and H. A. Zebker, "Mapping small elevation changes over large areas: Differential radar interferometry", J. Geophys. Res., 94(B7), pp. 9183-9191, 1989.

[17] R. F. Hanssen, "Radar Interferometry: Data Interpretation and Error Analysis", (Remote Sensing and Digital Image Processing), Springer, 2001.

[18] P. Berardino, G. Fornaro, R. Lanari, E. Sansosti, A New Algorithm for Surface Deformation Monitoring Based on Small Baseline Differential SAR Interferograms, IEEE Trans. Geosci. Remote Sens., 40 (11), pp. 2375-2383, 2002.

[19] Blanco-Sanchez P., J. Mallorqui, S. Duque, and D. Monnells, "The Coherent Pixels Technique (CPT): An Advanced DInSAR Technique for Nonlinear Deformation Monitoring", Pure and Applied Geophysics, 165(6), pp. 1167-1193, 2008.

[20] G. Fornaro, A. Pauciullo, F. Serafino, Deformation Monitoring over Large Areas with Multipass Differential SAR Interferometry: a New Approach based on the Use of Spatial Differences, Int. Journal of Remote Sens., 30(6), pp. 1455-1478, 2009.

[21] A. Ferretti, C. Prati, F. Rocca, "Nonlinear Subsidence Rate Estimation using Permanent Scatterers in Differential SAR Interferometry", IEEE Trans. Geosci. Remote Sens., 38, pp. 2202-2212, 2000.

[22] Ferretti, A., C. Prati, and F. Rocca, "Permanent Scatterers in SAR interferometry", IEEE Trans. Geosci. Remote Sens., 39(1), pp. 8-20, 2001.

[23] E. Sansosti, P. Berardino, M. Manunta, F. Serafino, G. Fornaro, "Geometrical SAR Image Registration", IEEE Trans. Geosci. Remote Sens, October 2006, Vol. 44, No. 10, 2861-2870.

[24] Golub G. H., C. F. Van Loan, "Matrix Computations", Johns Hopkins Univ Pr., 1996.

[25] G. Fornaro, A. Pauciullo, D. Reale, "A Null-Space Method for the Phase Unwrapping of Multi-Temporal SAR Interferometric Stacks", IEEE Trans. Geosci. Remote Sens., 49(6), pp. 2323-2334, 2011.

[26] D. Reale, D. O. Nitti, D. Peduto, R. Nutricato, F. Bovenga, G. Fornaro, "Post-seismic Deformation Monitoring With The COSMO/SKYMED Constellation", IEEE Geosci. Remote Sens. Lett, 8 (4), pp. 696-700, 2011.

[27] N. D'Agostino, D. Cheloni, G. Fornaro, R. Giuliani, D. Reale, "Space-time distribution of afterslip following the 2009 L'Aquila earthquake", J. Geophys. Res., 117, B02402, doi:10.1029/2011JB008523, 2012.

[28] A. Ferretti, A. Fumagalli, F. Novali, C. Prati, F. Rocca, A. Rucci, "A New Algorithm for Processing Interferometric Data-Stacks: SqueeSAR", IEEE Trans. Geosci. Remote Sens., 49 (9), pp. 3460-3470, 2011.

[29] G. Fornaro, A. Pauciullo, D. Reale, S. Verde, "SAR Coherence Tomography: a New Approach For Coherent Analysis of Urban Areas", Proc. of 2013 IEEE Conf. on Geosci. and Remote Sens. (IGARSS 2013), pp. 73-76.